Nanoscale Pattern Extraction from Relative Positions of Sparse 3D Localizations

Supporting Information

Alistair P. Curd[1], Joanna Leng[2], Ruth E. Hughes[1], Alexa J. Cleasby[1], Brendan Rogers[1], Chi H. Trinh[1], Michelle A. Baird[3], Yasuharu Takagi[3], Christian Tiede[1], Christian Sieben[4], Suliana Manley[4], Thomas Schlichthaerle[5], Ralf Jungmann[5], Jonas Ries[6], Hari Shroff[7] and Michelle Peckham[1]*

[1]School of Molecular and Cellular Biology, University of Leeds, Leeds, LS2 9JT, United Kingdom

[2]School of Computing, University of Leeds, Leeds, LS2 9JT, United Kingdom

[3]Cell and Developmental Biology Center, National Heart, Lung and Blood Institute, National Institutes of Health, Bethesda, MD 20892, USA

[4]Laboratory of Experimental Biophysics, École Polytechnique Fédérale de Lausanne, BSP 427 (Cubotron UNIL), Rte de la Sorge, CH-1015 Lausanne, Switzerland

[5]Max Planck Institute of Biochemistry, 82152 Munich, Germany and Faculty of Physics and Center for Nanoscience, LMU Munich, 80539 Munich, Germany

[6]European Molecular Biology Laboratory, Cell Biology and Biophysics Unit, 69117, Heidelberg, Germany

[7]Laboratory of High Resolution Optical Imaging, National Institute of Biomedical Imaging and Bioengineering, National Institutes of Health, Bethesda, MD 20892, USA

Supplementary Information Text

MATERIALS AND METHODS

Experimental RPD calculation

A table of *XYZ* localizations was used to calculate the experimental RPD for a field of view (FOV) using PERPL software (*relative_positions.py*, Suppl. Software, Fig. 1). Distances between localizations in the chosen directions were output as a histogram using 1-nm bins to compare with model relative position distributions (RPDs) generated as described below.

In cases where the signal to noise ratio (SNR) was low (Figs. S6, S7), we used a kernel density estimate (KDE) of the RPD. The criteria for applying this smoothing was the incorrect fitting of high frequency bin-to-bin noise in the raw histogram as peaks corresponding to characteristic distances in a macromolecular structure. The fitting algorithm sometimes detected this noise confidently as narrow peaks in the RPD, but the width of the fitted peak was less than the precision of the SMLM experiment. Therefore, we rejected these fits as spurious and used a KDE of the RPD to obtain less biased results.

In single molecule localization data, each localized molecule has a position uncertainty, or localization precision, σ_{loc}. The smoothing kernel was the distribution of distances between two Gaussian localization distributions[1], calculated from an estimate of σ_{loc}. Thus, the KDE is equivalent to a sum of distance distributions that reflects σ_{loc}. However, a KDE step should not be included if SNR is sufficiently high (such that bin-to-bin noise does not obviously bias the fit).

***In silico* model structures**

A variety of information can be used to construct *in silico* candidate model structures. The appearance of the reconstructed image typically provides information about the symmetry of the structure, for example the rotational symmetry of structures such as nuclear pores. The appearance of peaks and their positions in the experimental RPD plot suggest components of the underlying structure and length scales for these. For example, the minor peak at ~40nm and a major peak at ~95nm in the experimental RPD for the nuclear pore (Fig. 2B). Finally, other data including published structures (e.g. from electron microscopy) for

related molecules or structures can be used to help choose candidate models.

To construct the model, typically, the coordinates of proteins in a candidate model for a complex were calculated in a function, using structural parameters (e.g. diameter, height) that can be varied by the fitting algorithm (see below). For instance, in the rotationally symmetric models of Figs. 1 and 2, the vertices $\mathbf{v}_i$ of the model structure with symmetry order N have coordinates

$$\mathbf{v}_i = \begin{bmatrix} x_i \\ y_i \end{bmatrix} = \frac{D}{2} \cdot \begin{bmatrix} \cos\left(\frac{2\pi i}{N}\right) \\ \sin\left(\frac{2\pi i}{N}\right) \end{bmatrix}$$

where i = (0, 1, …, N − 1) and D is the diameter of the model.

***In silico* model RPD construction**

3D (or 2D) model RPDs were calculated from the *XYZ* (*XY*) candidate models. First, relative positions (RPs) were calculated between relative positions in the candidate model. For instance, in the rotationally symmetric model of Figs. 1 and 2, 2D RPs were obtained as follows:

$$\mathbf{RP_0} = \mathbf{v_1} - \mathbf{v_0}$$
$$\mathbf{RP_1} = \mathbf{v_2} - \mathbf{v_0}$$
$$\mathbf{RP_2} = \mathbf{v_3} - \mathbf{v_0}$$
$$\dots$$

until 2D RPs were obtained between all pairs of vertices. The RPD can be visualized and processed with its full dimensionality or converted to distances for the analyses shown here.

To analyze distance distributions in the RPD, the distances were obtained over the desired *X*, *Y* and *Z* components of the RPs, e.g. Δ*XY* or Δ*Z*. For example, distances Δ*XY* in the rotationally symmetric model of Figs 1&2 were:

$$\Delta XY_0 = \sqrt{RP_{0_x}{}^2 + RP_{0_y}{}^2}$$
$$\Delta XY_1 = \sqrt{RP_{1_x}{}^2 + RP_{1_y}{}^2}$$

The 1D, 2D or 3D distances between target molecule coordinates in the *in silico* model were then broadened, assuming Gaussian distributions for localizations at those points[1], to give a realistic, parametric distribution of relative positions. A multiplying parameter for the

amplitude of the distance contributions is also included so that the model can fit to the scale of the distance distribution in the experimental data. For instance, for the contribution of a distance over a 2D plane in an *in silico* model, the discrete distance ΔXY_0 becomes a distribution of ΔXY distances:

$$f(\Delta XY) = A\left(\frac{\Delta XY}{\sigma^2}\right)exp\left(-\frac{\Delta XY_0{}^2 + \Delta XY^2}{2\sigma^2}\right)I_0\left(\Delta XY.\,\Delta XY_0/\sigma^2\right)$$

where I_0 is the modified Bessel function of order zero, A is the scaling multiplier and σ is the broadening on the discreet *in silico* distance, arising from variation in the real sample structure and precision of acquired data. When $\sigma^2 << \Delta XY_0{}^2$, we use the approximation[1]

$$f(\Delta XY) \approx A\left(\frac{1}{\sqrt{2\pi}\sigma}\right)\sqrt{\frac{\Delta XY}{\Delta XY_0}}exp\left(-\frac{(\Delta XY - \Delta XY_0)^2}{2\sigma^2}\right)$$

These contributions for all of the discrete distances in the candidate model (ΔXY_0, ΔXY_1, ΔXY_2, …) are summed to produce a combined distance distribution for the model. Two distance distributions for Gaussian clusters with a mean distance of zero (replacing ΔXY_0 with 0 above) were also included to model repeated localizations of the same molecule and unresolvable substructure at a point in the *in silico* model. This can also be considered as equivalent to a spread of mislocalizations resulting from overlapping images of nearby emitters[2]. An example of the presence of repeated localizations of the same molecule is the peak at ΔXY < 10 nm in the experimental Nup107 RPD data in XY (Fig 2B) (and see further explanation below).

Generally, noise in the localization data (e.g. due to finite localization precision or residual inaccuracy in frame-to-frame drift correction, after drift correction has been applied to the SMLM image sequence) increases the broadening parameters in the model. Where localization precision is estimated in a model, this includes the effect of such noise.

At least three options are available to include further aspects of variability (e.g. of diameter of a ring or random placement of localizations around a ring). First, a parameterized modification to the *in silico* model RPD can be used, as in the smoothing of ΔXY and the treatment of repeated localizations, above. Second, additional localization positions can be calculated for the candidate

in silico structural model, before calculating the RPD. This approach also requires a parametric model of variability, but this may be more easily derived from assumptions at the initial structural stage. It also requires calculating the positions of enough localizations to represent their distribution faithfully for the subsequent RPD calculation, and will increase the time taken to calculate RPDs, including during iterations of model fitting. Finally, a total RPD can be generated from a concatenation of RPs calculated from several structural models, e.g. from rings of different diameters, where diameter is assumed to vary in a parameterized way. Background terms can also be included, appropriate to the experimental conditions and acquired data, as a further linear addition to the distance distribution obtained from the *in silico* model RPD. For instance, for a random distribution of 2D localizations, a background distance function

$$BG(\Delta XY) = C.\Delta XY$$

would be added, where C is a scaling multiplier to allow fitting to the experimental data. In the *XY* Nup107 data (Fig. 2), we noted that this background distribution would be modified by the fact that the ring-like structures do not overlap, and the low density of localizations observable within the rings. We therefore used an approximate background distribution of

$$BG(\Delta XY) = \begin{cases} 0, & \Delta XY < onset \\ C.\Delta XY - C.onset, & \Delta XY \geq onset \end{cases}$$

where *onset* is a distance at which $BG(\Delta XY)$ begins to increase linearly as expected for a random distribution of localizations. This model provided a good fit to the data (Fig. 2E). In total, therefore, this model had 9 parameters to vary in the fitting procedure: D, σ, A, C, *onset*, equivalents to σ and A for repeated localizations of the same molecule, and equivalents to σ and A for unresolvable substructure at a point in the *in silico* model structure.

Quantitative model selection using the corrected Akaike's Information Criterion (AICc)

We used Akaike's Information Criterion (*AIC*)[3-5] to determine which candidate model RPD best fits the experimental RPD. The *AIC* value for the best model is lower compared to the other models, which means that less information is lost when approximating the data with that model. The *AIC*

includes a penalty for increasing the number of parameters (*K*) in a model, which disfavors over-fitting by complex models as the number of parameters increases. To improve our method further, we based model selection on a corrected *AIC* (*AICc*) value that further increases the penalty for increasing *K*, as *K* becomes non-negligible with respect to the number of data points (e.g. distance histogram bins) [4, 6]:

$$AIC = n\ln\left(\frac{SSR}{n}\right) + 2K$$

and

$$AICc = AIC + \frac{2K(K+1)}{n-K-1}$$

where *n* is the number of data points, or distances at which the model and experimental RPDs are evaluated, *SSR* is the sum of squared residuals for the fitted model and *K* is the number of estimated parameters in the model fit. In this case (least-squares fitting), *K* is the number of fitted parameters used in the calculation of the *in silico* model RPD plus one, to include the estimate of the variance of the residuals. Therefore *K* = 9 + 1 = 10 was used in the comparison between fitted models with different orders of symmetry against the Nup107 Δ*XY* data.

Differences in *AICc* values are used in calculations of relative likelihood that the candidate model RPDs are correct, given the data[4, 7]:

$$\text{likelihood} \propto e^{-\frac{1}{2}AICc}$$

Likelihood ratios resulting from differences in *AICc* values can also be given as relative 'Akaike weights', *w*, in a sum to 1, to aid interpretation[4, 5]. Among the models being compared, model *i* has *AICc* value $AICc_i$, and the most likely model has the minimum *AICc* value, $\min(AICc_i)$. Then each model *i* has an *AICc* difference,

$$\Delta_i = AIC_i - \min(AICc_i)$$

and an Akaike weight,

$$w_i = \frac{exp(-\Delta_i/2)}{\sum_i exp(-\Delta_i/2)}$$

Note that while this approach is able to demonstrate which of the candidate models best fits the data, it does not unequivocally prove that the model with the lowest *AICc* value represents the true arrangement of the molecules. In the derivation of *AIC*[4], it is assumed that information will

be lost between the complexity of the data obtained on the true molecular arrangement (including natural variability and contributions to noise) and the model approximating that arrangement, but it is not possible to quantify that information loss absolutely[4, 5].

AIC does, however, give the difference in information loss between models, and so provides relative information on how good the models are compared with one another, as explained above. Inspection of the model fits to the experimental data provide further useful information to the user as to how well the best model or models are explaining the data. Furthermore, as data leading to improved hypotheses of structure become available, and as data collection techniques improve, *AIC* may later be used to identify a new model as an improvement on the previous best. If models result in similar *AICc* values and Akaike weights, the user should not confidently select one model over another, i.e. among the linear models shown in Table S7. However, some data and *in silico* models may be separated into different dimensions (e.g. Δ*XY*, Δ*Z*; Figs. 2, 4), and model selection may still proceed using the RPD component in one dimension (or combination of dimensions), even if it does not yield a single most-likely model in another. Furthermore, if the RPD appears similar to a random, or otherwise simply explained distribution, these types of distributions should be included as controls, to judge whether the proposed structural models are really any more likely to be true than a random distribution. It was necessary to take such an approach in the investigation of ACTN2 localizations, where we compared *in silico* models of organized structure with a random distribution of localizations across the thickness of the Z-disc (Fig. 4A,B, Table S7).

Notes on specific *in silico* models

Nup107

In the Nup107 *XY* model (Fig. 2C–F), the sharp peak in the RPD at < 10 nm led us to include the term for repeated localizations, resulting from multiple on/off cycles of a single Alexa Fluor 647 molecule in dSTORM. The trough in the RPD between the first two peaks was fitted poorly until an additional term for unresolvable substructure at points on the model was also included. This is consistent with

previous EM data [8] that shows substructure at each vertex of the complex.

The RPD has a linear form beyond ~150 nm, as expected for a distribution of localizations in 2D, beyond the length scale of the visible features (Fig. 2A, B). The background term for RPs from localization data internal to a single ring structure is expected to be lower than the contribution from adjacent ring structures. This explains why an extrapolation of the linear form (background term) of the RPD beyond ~150 nm does not intersect with the origin.

We approximated the background of RPs using a two-segment linear model, with the RPD equal to zero up to an onset distance (variable parameter) and increasing with a linear slope beyond that. Mathematical details are given for this model above. Free parameters in model fitting include diameter of the ring, broadening and amplitude of the inter-vertex distance contributions to the RPD and broadening, amplitude of the term for repeated localizations of a molecule, amplitude of the unresolvable substructure term, and the onset distance and slope for the background mode.

In the *Z* model for Nup107 (Fig. 2J–M), the peaks in the RPD were explained well with only one broadening parameter for the within-layer spread of localisations. Note that the precision of localization in *Z* is expected to be 2–3 times larger than in *XY*. Here we used a background term for RPs with an exponential decay. This is derived from the form of the evanescent field in Z used to excite the fluorescent labels.

DNA Origami

In the DNA-origami model, a model that included two terms for zero mean distance (for repeated localizations of the same molecule and for unresolvable structure; Fig. S4) was a better fit than a model with only one such term, according to the AICc. This seems reasonable as the nanostructures contain multiple labelling sites in a cluster at each vertex, as described previously[9] and each of these sites were localized repeatedly by DNA-PAINT [10]. We used a linear background model for the RPD as would be expected for 2D data. We made this approximation for this 3D dataset because the data was greater in extent in *XY* than in *Z* and because the exponential decay of the excitation field in *Z* reduces the number of RPs as ΔZ increases. To take account of nearby structures on the square lattice that is visible in the data, we included a

term with equal contributions at distances of *a* and √2 × *a*, where *a* is the lattice constant of the square grid.

ACTN2

In the Z-disc ACTN2 *X* model (Figs. 4, S6D), the contributions of the repeating distance units decrease linearly with the number of repeats between localizations, as expected if ACTN2 is on a regular repeat and populates all of the binding sites in a repeating structure (or populates them randomly). For instance, in the five-layer Z-disc *in silico* model structure, containing four multiples of the repeating distance *r*, the relative amplitudes of the contributions at distances *r*, 2r, 3*r and 4r* are 1, 0.75 (1 – 1/4), 0.5 (1 – 2/4) and 0.25 (1 – 3/4). We also included repeated localizations of the same Alexa Fluor 647 molecule. The background term is the decreasing linear distribution expected for localizations in a 1D random uniform distribution with finite bounds.

In the Z-disc ACTN2 *YZ* model (Figs. 4, S7E), we used a standardized experimental RPD, which is defined as the RPD (at distances Δ*YZ*) divided by Δ*YZ* (Fig. S7). A random distribution of distances in 2D would result in a constant value for the standardized RPD. Therefore, we used a constant background term.

Fitting *in silico* model parameters

The model RPDs were fitted to the experimental distance distribution in Python scripts with *scipy.optimize.curve_fit* [11], a least squares fitting function. Where raw distance histogram bin values were large (Figs. 2, 3), we scaled the counts to have a mean of 1.0, to improve the performance of the fitting algorithm. This function outputs the covariance matrix for the optimized model parameters, cov(**P**), where **P** is the vector of *in silico* model parameters. Uncertainties on parameters (1 s.d., given as variation in the last significant digits) are √diag(cov(**P**)). Confidence intervals on the model RPD values at each distance were calculated from cov(**P**) and derivatives of the fitted model values with respect to the model variables:

$$\sigma^2 = \mathbf{J}\,\mathrm{cov}(\mathbf{P})\,\mathbf{J}^T$$

where σ^2 is the variance of the fitted model RPD and **J** is the Jacobian of **P**. **J** was calculated with *numdifftools*, a Python package based on the MATLAB toolbox *DERIVESTSuite* (John D'Errico,

2006, http://www.mathworks.com/matlabcentral/fileexchange/13490-adaptive-robust-numerical-differentiation). Bounds on the 95% confidence intervals are the estimated model RPD value ± 1.96σ.

Starting values and bounds for parameters (e.g. distances, broadening on the distribution) are also required by the model-fitting implementation. Examples of these, including default values and opportunities to edit them, are available in the code. For instance, for the rotationally symmetric models of *rot_2d_symm_fit.py*, they can be seen in the functions *create_default_fitting_params_dicts*, *set_up_model_replocs_substruct_iso_bg_with_onset_with_fit_settings* and *set_up_model_replocs_substruct_no_bg_with_fit_settings*.

Code availability

The code developed in this study is available at https://bitbucket.org/apcurd/perpl-python3/src/0.1/, and test data for the software can be found at https://bitbucket.org/apcurd/perpl_test_data/src/0.1/. Included with the code are interactive notebooks that run analysis and produce plots and results as reported. Updated versions of the code can be found at https://bitbucket.org/apcurd/perpl-python3/.

3D dSTORM localizations of SNAP-tagged Nup107. Data was acquired as described in Li et al. [12]. U2OS cells that expressed Nup107–SNAP [13] were fixed and labelled with benzylguanine-Alexa Fluor 647 (NEB, Ipswich, MA, USA) and imaged on a custom microscope in a standard blinking buffer (50 mM Tris, pH 8, 10 mM NaCl, 10% (w/v) d-glucose, 35 mM 2-mercaptoethylamine, 500 µg/mL glucose oxidase, 40 µg/mL catalase, 2 mM cyclooctatetraene. Single molecules were localized using a Gaussian PSF model and the data were drift corrected using redundant cross-correlation.
We filtered the localizations for high precision, less than 10 nm uncertainty in Z according to the MLE fitting routine [12].

3D DNA-PAINT localizations of DNA-origami structures. DNA origami nanostructures were assembled in a one-pot reaction in a final volume of 50 µl. The assembly mix contained p8064 single-stranded DNA scaffold strand (Tilibit Nanosystems) at a final concentration of 10 nM, single-

stranded core DNA oligonucleotides at 100 nM, DNA-PAINT P1 (5'-Staple-TT ATACATCTA-3') docking sites at 500 nM, biotinylated DNA strands at 800 nM in a buffer of 5 mM Tris and 1 mM EDTA supplemented with 12 mM $MgCl_2$. The pooled strand solution was heated to 80 °C for 5 min followed by a thermal ramp from 60 °C to 4 °C over the course of 17 h. Assembled nanostructures were purified by agarose gel electrophoresis (1.5 % (w/v) agarose, 0.5×TAE, 10 mM $MgCl_2$, 1×SYBR Gold) at 3 V/cm for 3 h at 4 °C. Gel bands were cut, crushed and structures were purified with Freeze 'N Squeeze spin columns (Bio-Rad) for 5 min at 1,000×g at 4 °C.
For DNA-PAINT imaging, flow chambers for imaging were assembled with a coverslip (no. 1.5, 18x18 mm^2) attached to a standard microscopy glass slide with two strips (approximately ~0.5 cm – 1 cm apart) of double-sided sticky tape. As a first step, 20 µl of biotin-labeled bovine serum albumin (1 mg/ml, dissolved in buffer A (10 mM Tris-HCL, pH 7.5, 100 mM NaCl and 0.05% (v/v) Tween 20, pH 7.5)) was flown into the flow chamber and incubated for 2 min. Afterwards, the chamber was washed with 40 µl of buffer A, followed by incubation with 20 µl streptavidin (0.5 mg/ml in buffer A) and incubated for another 2 min. After washing with 40 µl of buffer A and 40 µl of buffer B (5 mM Tris-HCl, pH 8, 10 mM $MgCl_2$, 1 mM EDTA, 0.05 % (v/v) Tween 20 at pH 8). 200 pM of the self-assembled DNA origami structure was incubated in the channel and allowed to attach for 2 min. The chamber was washed with 40 µl of buffer B and finally 3 nM Cy3b labeled DNA-PAINT imager strand (CTAGATGTAT-Cy3b) was added in buffer B supplemented with a PCA/PCD/Trolox oxygen scavenging system. The chamber was sealed with picodent before imaging. Nanostructures were imaged for 15000 frames, with an exposure time of 200 ms per frame and at a laser excitation (560 nm) intensity of 3 kW/cm^2.

DNA-PAINT imaging was carried out on an inverted Nikon Eclipse Ti microscope (Nikon Instruments) with the Perfect Focus System, applying an objective-type TIRF configuration with an oil-immersion objective (Apo SR TIRF 100×, NA 1.49, Oil). A 561 nm excitation laser (200 mW, Coherent Sapphire) was used. The laser beam was passed through a cleanup filter (ZET561/10x, Chroma Technology) and coupled into the microscope objective using a beam splitter (ZT561rdc, Chroma Technology). Fluorescence light was spectrally filtered with an emission filter (ET600/50 and ET575lp for

561 nm excitation, Chroma Technology) and imaged on a sCMOS camera (Andor Zyla 4.2) without further magnification, resulting in an effective pixel size of 130 nm after 2x2 binning. A cylindrical lens was inserted into the beam path in front of the camera for 3D imaging, the corresponding calibration was performed as previously reported [14]. Camera Readout Sensitivity was set to 16-bit, Readout Bandwidth to 200 MHz.

DNA-PAINT images were reconstructed with the Picasso software suite as previously reported [10]. Single structures were picked and aligned in their native orientation in a two-dimensional grid for further processing. This grid of structures was the FOV analyzed with PERPL (**Fig. 2g–j**), without prior knowledge of the origami structure or its arrangement. Localizations were not filtered for estimated localization precision in this case.

Z-disc protein localization with 3D dSTORM.

Z-disc proteins were imaged either using 3D dSTORM, using an Affimer to ACTN2. Affimers are small (~10kDa) non-antibody binding proteins that can be used like antibodies, but with the advantage that their small size reduces linkage error in 3D dSTORM [15, 16]. To obtain Affimers to ACTN2, the CH domains from human ACTN2 were expressed and purified from *E.Coli* as described [17], biotinylated, and used in a phage-display screen as described [18]. All 7 unique Affimers obtained from the screen were expressed, purified, and directly dye labelled (either using Alexa Fluor 647, or Alexa Fluor 488) using the unique C-terminal cysteine as described [19]. The dye-labelled Affimers were then tested for their ability to label Z-discs in fixed adult rat cardiomyocytes by confocal microscopy (outlined below). Those that did were then tested in dSTORM (using Alexa Fluor 647 labelled Affimers). The Affimer that demonstrated the best labelling for dSTORM was then used in subsequent experiments.

To prepare cells for 3D STORM imaging, isolated cardiomyocytes were prepared as described [20] on laminin-coated cleaned 25-mm diameter, #1.5 (Scientific Laboratory Supplies, MIC3350) coverslips [21]. Cells were allowed to attach in cardiomyocyte medium [20] for 1-2 hours at 37 °C before fixing with freshly made 2% paraformaldehyde (PFA) in phosphate buffered saline (PBS)(for dSTORM). Fixed cells were permeabilized with 0.5% Triton X-100 in PBS,

blocked with 5% bovine serum albumin (BSA) in PBS for 1 hour, and then stained with Affimers directly labelled with Alexa-647 on a unique C-terminal cysteine residue ([16, 22]. The stock Affimer was diluted 1/750 in PBS with 1% BSA to give a final concentration of 0.6 µg/ml, for 60 mins at room temperature. After staining, cells were washed in PBS and stored briefly in PBS at 4°C before 3D dSTORM imaging. Imaging for 3D dSTORM [23] used an inverted microscope (Olympus, IX81) with a 60x, 1.2 NA, water-immersion objective lens (Olympus, UPLSAPO60XW). An automated *XY* stage with additional piezoelectric adjustment in *Z* (PZ-2000, Applied Scientific Instrumentation) was fitted to accommodate a focus lock (C-focus, Mad City Labs) and the sample. The coverslips were mounted in chambers (I-3033-25D, Applied Scientific Instrumentation), held in a stage insert (I-3033, Applied Scientific Instrumentation). Lasers at 561 nm and 405 nm (Jive, Cobalt and LuxX, Omicron, respectively, integrated in a LightHUB, Omicron) provided widefield excitation, together with a custom-built 2x beam expander before the rear illumination port of the microscope. A multi-band excitation filter (zet405/488/561/640m, Chroma) was used with a multi-band beamsplitter (zt405/488/561/640rpc, Chroma) and a multi-band emission filter (zet488/561/640m-TRF). The imaging path included a 1.6x magnifier internal to the microscope, an external 1.2x magnifier (Diagnostic Instruments, DD12BXC) and a cylindrical lens with f = 150 nm (Thorlabs, LJ1629RM-A), which provided an astigmatic point-spread function for a single emitter [14]. Images were captured by a back-illuminated, electron-multiplying CCD camera, cooled to −80°C (Andor Technology, iXON Ultra, model DU-897U-CSO-#BV), using published scripts [23] called from the camera interface (Andor Technology, SOLIS).

The data acquisition workflow [23] included capture of calibration images of a gold nanoparticle (742031, Sigma-Aldrich) in steps of 50 nm in *Z* over a 4 µm range and use of these particles for drift-tracking. The Alexa Fluor-647 labelled Affimer to ACTN2 was imaged in imaging buffer composed of PBS, pH 8.0 with 10% glucose (w/v), 0.5 mg/ml glucose oxidase, 80 µg/ml catalase, 110mM β-mercaptoethanol. The fluorophore was excited using a 642-nm laser (100 mW), with EMCCD gain 150, and the blinking rate was controlled by gradually increasing 405 nm laser power from 2-20 mW. At least 11,000 frames were collected at 20

Hz and acquisition was stopped when the number of emission events per frame became negligible. Jump tracking was used to image the fiducials at the coverslip surface as well as emission events at a different height within the cell, so that both images fit within the calibration series. Emission events were localized using *palm3d* [23], with those lasting for more than one frame averaged to provide one 'linked' localization. Localizations were then binned into a histogram for display, accounting for drift and *XY* distortion by the cylindrical lens. In order to make the localization data available for analysis, new Python scripts were required, which are available at https://bitbucket.org/apcurd/palm3d_extra/. These scripts provide users of *palm3d* with corrected localization data, including a precision estimate, allowing filtering and subsequent analysis of the dataset. They are for use with Python 2.7, for compatibility with *palm3d*.

Localization precision was estimated as the standard error on the localization position ($\sigma / \sqrt{N}$), using a 2D Gaussian fit of the relevant image from the *palm3d* calibration stack (σ, mean of two widths from the 2D fit) and the photon count above background (N, available from the *palm3d* data for every linked localization). This simple precision estimate is likely to be an under-estimate [24], but was useful as a method to allow filtering for higher-precision localizations and to assist in the resolution of short distances within the complex (e.g. ~20-nm distances between ACTN2 localizations). We filtered for estimated localization precision within 5 nm.

3D SMLM fields of view (ranges of localization coordinates) were cropped such that gold nanoparticles, used for drift tracking, were excluded. A maximum pairwise distance of 200 nm was used in PERPL, so that distances across the thickness of the Z-disc would be obtained. 3D SMLM cardiomyocyte reconstructions, and the corresponding sets of 3D relative localization positions, were aligned by first rotating an *XY*-projection of each cell reconstruction (e.g. Fig. 2A) such that the cell-axis pointed along *X*. The corresponding set of 3D relative localization positions was then rotated by the same angle.

Validation of the ACTN2 Affimer by staining and structure determination.

We screened for Affimers to ACTN2 and identified the best Affimer for imaging by confocal microscopy of fixed cardiomyocytes prepared in the same way as for dSTORM, except high concentrations of Affimer (Alexa 647 or 488 dye labelled) was diluted 1/100 from stock. Fixed cardiomyocytes were co-stained with anti-ACTN2 antibody (1:400) (Sigma, A7811, lot no. 024M4758), followed by staining with Alexa Fluor 647 (or 488) -labelled donkey anti-mouse secondary antibody (1:100, ThermoFisher). All antibodies and dyes were diluted in 0.2% BSA. Coverslips were washed and mounted in Prolong Gold Antifade. Cells were imaged using a 63x objective (NA 1.4), on a Zeiss 880 LSM Airyscan confocal microscope.

To determine where the Affimer interacts with ACTN2 CH domains, we performed X-ray crystallography with the complex. Crystals were obtained at 20°C by the sitting-drop vapor diffusion method using 20% (w/v) polyethylene glycol 3350 and 0.2 M ammonium tartrate with a protein concentration of 8 mg ml^{-1}. The crystals were flash-cooled in liquid nitrogen after soaking for 30 seconds in mother liquor solution containing 25% (v/v) glycerol as a cryo-protectant. X-ray diffraction data were collected at the Diamond Light Source on beamline I04 to 1.2 resolution at 100 K. The diffraction images were indexed and integrated using DIALS [25] before subsequent scaling in AIMLESS [26] and data processing in the CCP4i2 suite [27].

The unit cell parameters for the crystal are a=46.2Å, b=48.5Å, c=147.0Å, α=β=γ=90.0° in space group $\boldsymbol{P}2_12_12_1$ with one ACTN2:AF9 complex in the asymmetric unit cell. The structure was determined by molecular replacement using the program PHASER [28] with the human ACTN2 CH domain structure (PDB code 5A38 [17]) and the truncated Affimer (PDB code 4N6T [29]) as the search models. Initial rounds of automated model building were performed in BUCCANEER [30] followed by iterative rounds of manual model building in COOT [31] and refinement using REFMAC5 [32]. During the course of the model building structural validations were carried out using the program MOLPROBITY [33]. The N-terminal 16 residues and C-terminal 13 residues of the human ACTN2 CH domains were disordered and were not included in the final refined structure. The structure factor and coordinate files have been deposited in the Protein Data Bank with accession code 6SWT. The structure shows that the Affimer interacts with a loop in CH domain 2.

Estimates of Z-disc structure localization efficiency.
We roughly estimated the number of Z-disc lattice points in the FOV (ACTN2 Affimer 3D dSTORM) by dividing the acquisition volume by the lattice dimensions. Acquisition volume ≈ number of Z-discs imaged × ~100 nm Z-disc thickness × ~15 µm cell-width × ~2 µm acquisition depth (range of localizations in *Z*). *Z*-disc lattice dimensions are ~20 nm (cell-axial, *X*) × ~17 nm × ~17 nm (cell-transverse, *YZ*) [34]. The localization efficiency for ACTN2 was obtained by dividing this result by two, since the labelled domains are found in pairs separated by only ~3 nm along the actin filaments of the Z-disc lattice, binding either side of the filament. Each pair is considered to be at the same lattice point, or within the resolvable length scale of these experiments.

2D dSTORM localizations of Cep152.
Human centrioles were purified and antibody labelled as described previously [35]. STORM imaging of immunostained centriole samples was performed using a recently developed flat-field epi illumination microscope [36]. Briefly, a 642 nm laser (2RU-VFL-P-2000-642-B1R, MPB Communications) was used to switch off fluorophores on the sample, while a 405 nm laser (OBIS, Coherent) controlled the return rate of the fluorophores to the fluorescence-emitting state. A custom dichroic (ZT405/561/642/750/850rpc, Chroma) reflected the laser light and transmitted fluorescence emission before and after passing through the objective (CFI60 PlanApo Lambda Å~60/NA 1.4, Nikon). After passing the emission filter (ET700/75M, Chroma), emitted light from the sample was imaged onto the sCMOS camera (Prime, Photometrics). Axial sample position was controlled using the pgFocus open hardware autofocus module (http://big.umassmed.edu/wiki/index.php/PgFocus). Typically, 40,000 frames at 10 ms exposure time were recorded using Micromanager [37]. Imaging was performed using an optimized STORM buffer as described previously [38]. Image stacks were analyzed using a custom CMOS-adapted analysis routine [39]. Localizations from individual centrioles were segmented and extracted using SPARTAN as described previously [35]. We filtered the localizations for high estimated localization precision, within 5 nm. Segmented and filtered particles were averaged as described previously 35.

SUPPLEMENTARY FIGURES

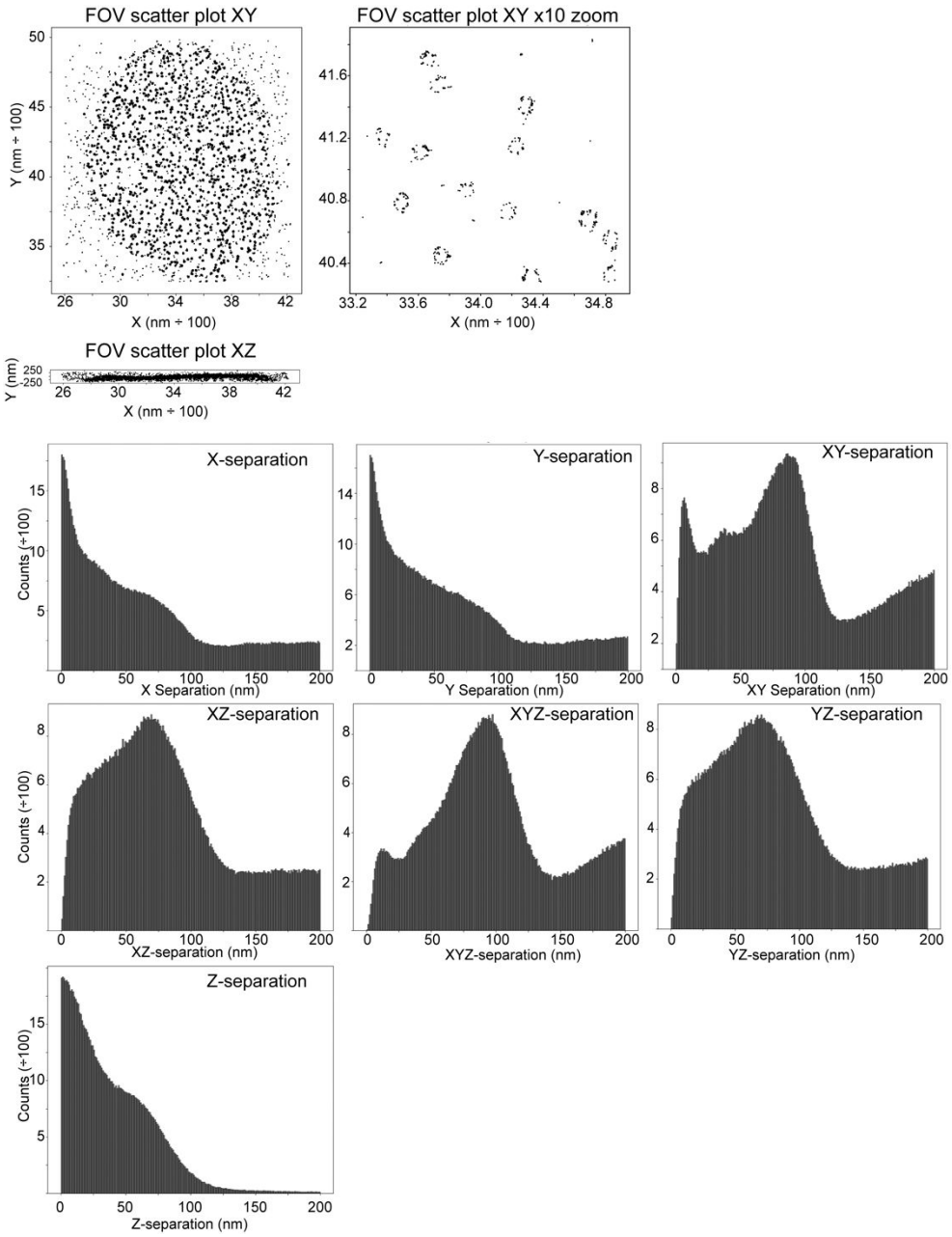

Fig. S1. Example Scatterplots of the localizations in *XY* and *XZ* and the distance histograms that can be generated in various directions when *relative_positions.py* is run on a list of localizations. These are placed into an html report for the user, as well as being saved individually.

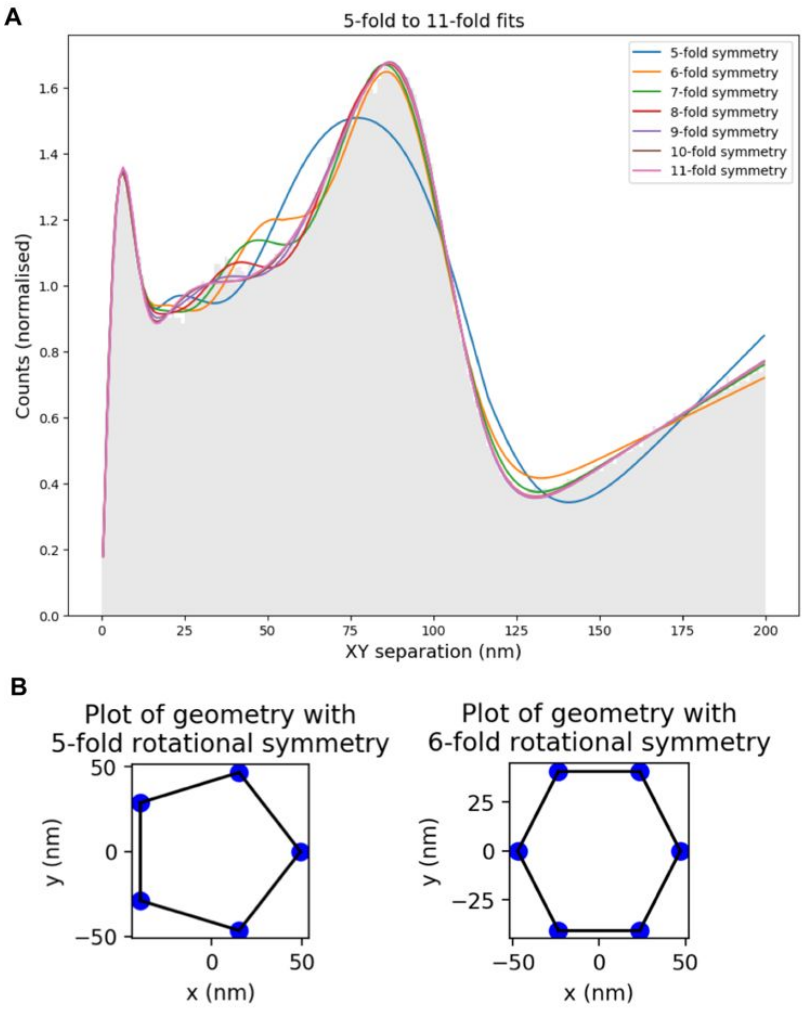

Fig. S2. Examples of plots saved (A) and contained in the html report when *rot_2d_symm_fit.py* (see note on code availability) is run on output data from *relative_positions.py*. In this example, the optimized models for each order of symmetry are plotted on the *XY*-distance histogram (A) and simple plots of the optimized geometry at each order of symmetry are generated (B). These examples are models fitted to the Δ*XY* distribution for Nup107 localizations in Fig. 2A–G. The html report from *rot_2d_symm_fit.py* also contains the AICc values, relative likelihoods, and parameter estimates and uncertainties for each modelled order of symmetry. Additionally, it contains descriptions of the model parameters and their initial guesses and bounds as used by the least squares fitting function.

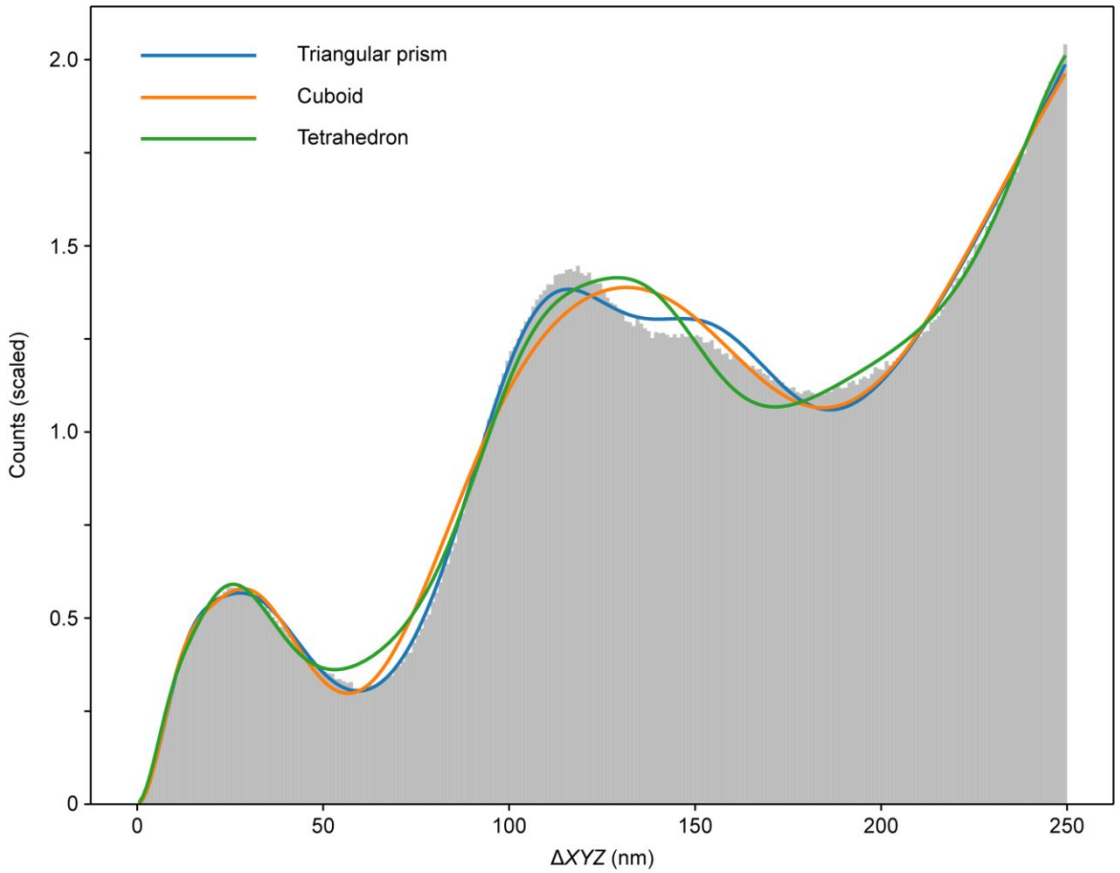

Fig. S3. RPD models fitted to the distance histogram of localizations of dye labels on a DNA origami structure (Fig. 3, Tables S4, S5). Two triangular prism models follow the same curve: in one the sides are all equal, in the other the length of the edges on the equilateral triangular faces was independent of the length of the connecting edges between them. In the cuboid model, the three edge lengths were independent of each other. In the tetrahedron model, the edge length on the equilateral triangular base was independent of the height of the pyramid.

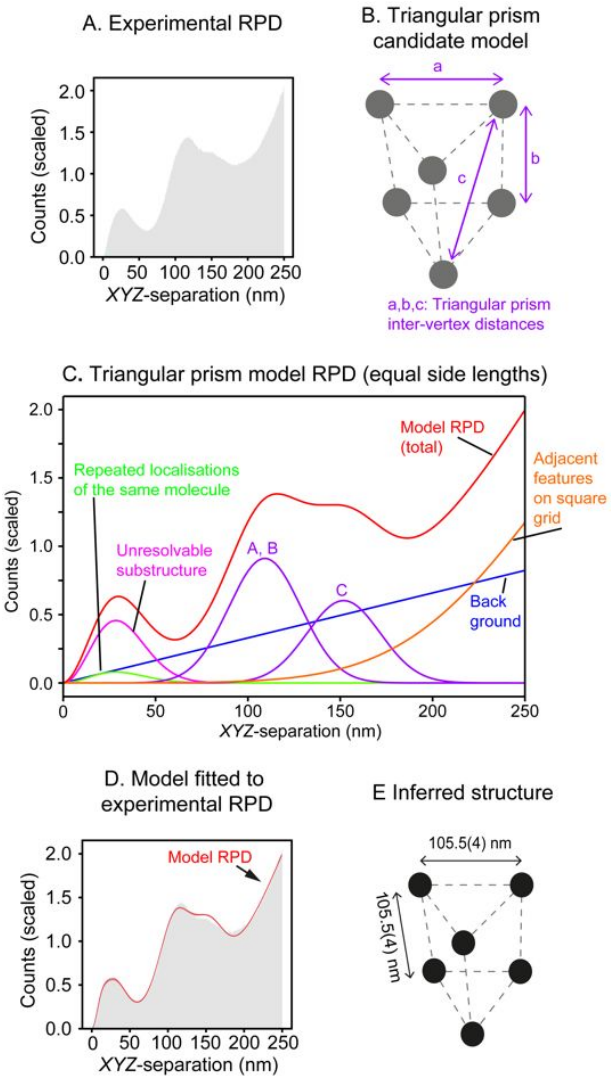

Fig. S4. Generation of the model RPD for triangular prismatic structures on a square grid, and fitting to the experimental distribution of localizations on DNA-origami, obtained with DNA-PAINT[10]. Histogram of separations between localizations in 3D Euclidean space (A). Equilateral triangular prismatic candidate structure for a geometry arranged on a square grid (B). RPD generated from the model in B, when distances a and b are equal (C); this also includes the terms shown for repeated localizations of the same molecule, unresolvable substructure or clustering, background and a contribution from features nearby on the square grid, i.e. on adjacent grid points (see Material and Methods). The model RPD fitted to the experimental distribution (D), 95% confidence interval in pink (too

narrow to see at this scale). The structure inferred from fitting the *in silico* model RPD to the experimental relative position data (E).

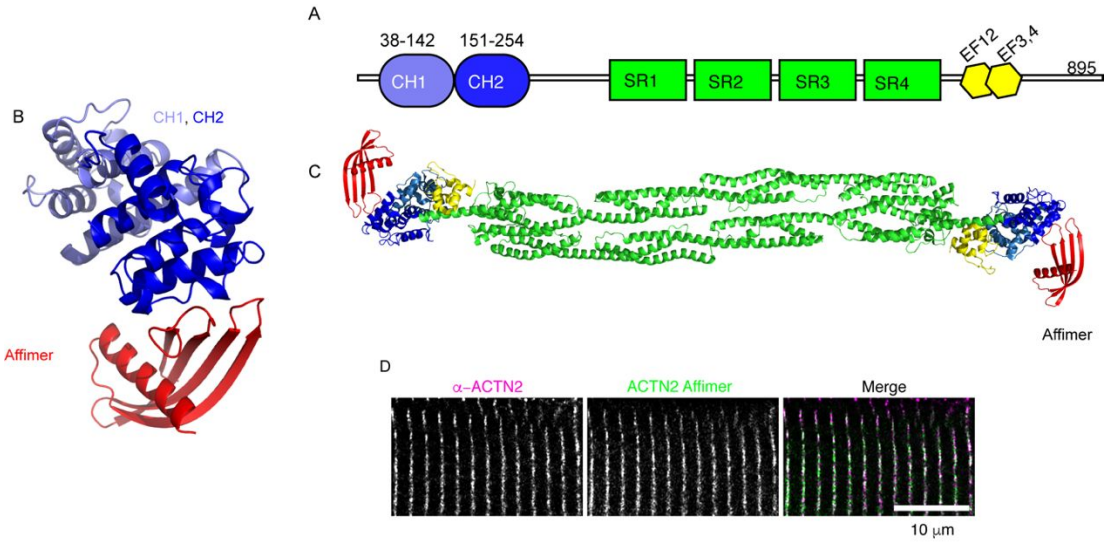

Fig. S5. Affimer used to stain ACTN2 in the Z-disc. The CH domains of α-actinin-2 (ACTN2) (A) were used to generate an Affimer. The co-crystal of the Affimer and the CH domains (B) shows that the Affimer binds to a loop in CH2. This places the Affimer at either end of the antiparallel dimer (C). D: Confocal microscopy using adult rat cardiomyocytes shows the ACTN2 Affimer, labelled on a unique cysteine (C-terminal) with Alexa 647, is localized to the Z-disc, similar to that for the antibody to ACTN2 (α-ACTN2).

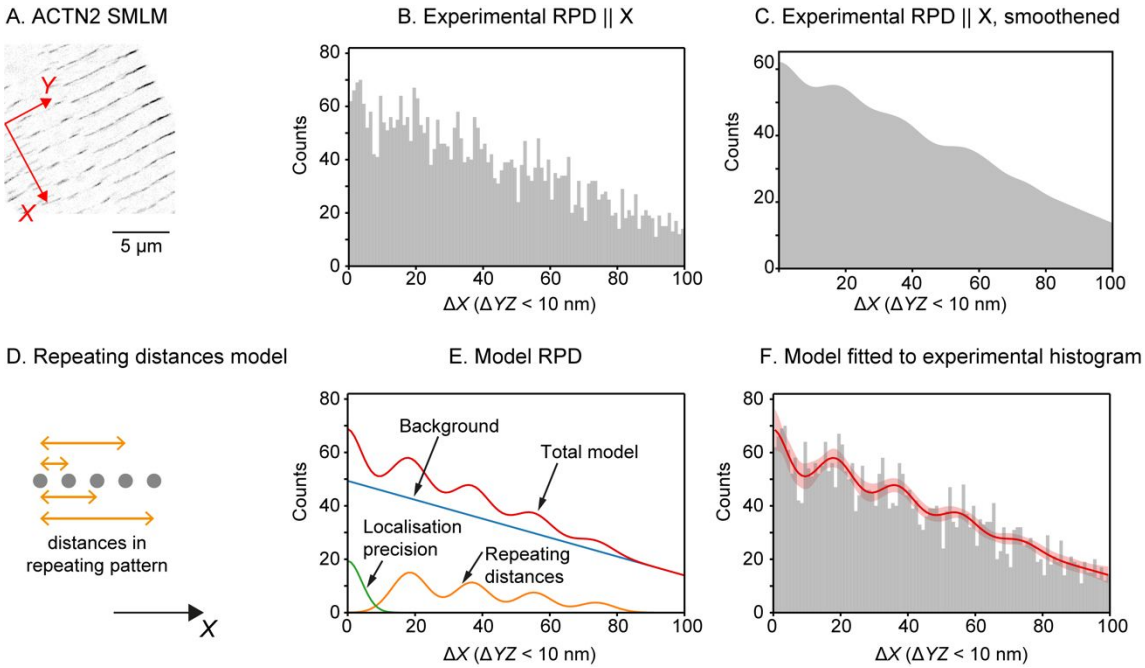

Fig. S6. Workflow for PERPL analysis of relative positions parallel to the cell axis (*X*) in ACTN2 Affimer dSTORM data. Reconstruction of the FOV, from ACTN2 localizations (A). Experimental distance histogram in *X*, including only pairs of localizations for which $\Delta YZ \leq 10$ nm (B). Kernel density estimate (KDE) (C) of the distribution of ΔX. The kernel has the form of the distance distribution between two Gaussian distributions in 1D ([1], Materials and Methods), with $\sigma = 3.1$ nm for the Gaussian distributions (mean localization precision for included localizations (Materials and Methods)). Illustration of distances in a candidate model structure for localizations on a simple linear repeating pattern (D). The RPD for a model structure containing five localizations on a linear repeat, also including a background term for random localizations across the finite thickness of the Z-disc and a localization precision term for repeated localizations of the same molecule (E). The model of E fitted to the experimental data, 95% confidence interval in pink (F).

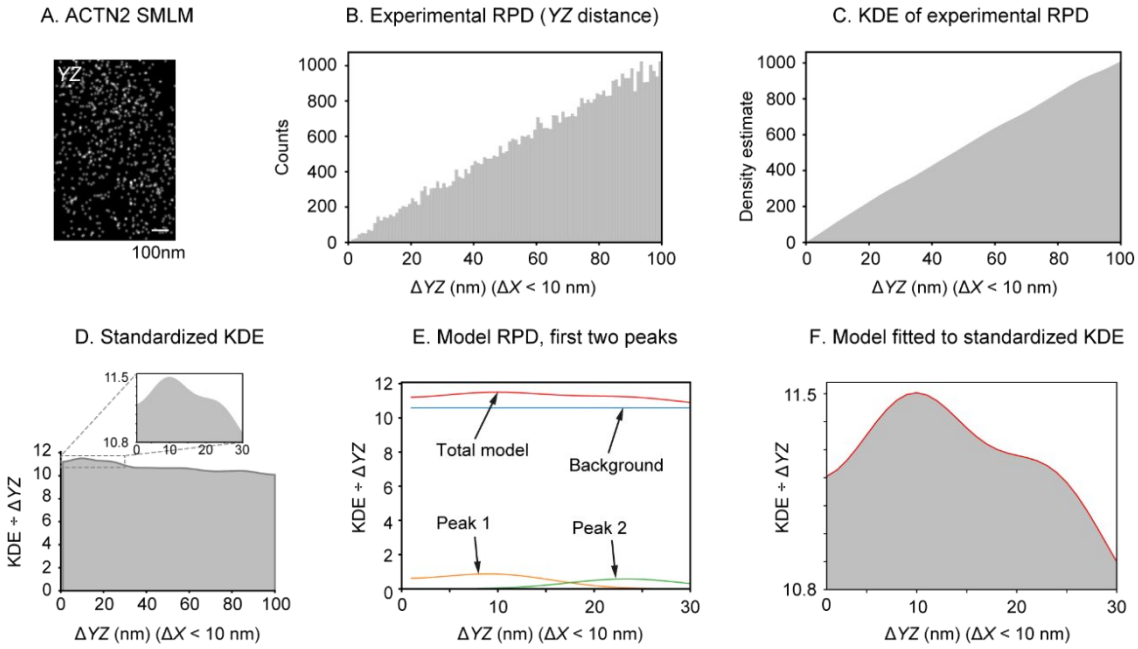

Fig. S7. Workflow for PERPL analysis of relative positions perpendicular to the cell axis (*X*) in ACTN2 Affimer dSTORM data. Reconstruction of the FOV from ACTN2 localizations (A). Experimental distance histogram in *YZ*, including only pairs of localizations for which $\Delta X \leq 10$ nm (B). KDE (C) of the distribution of ΔYZ. The kernel has the form of the distance distribution between two Gaussian distributions in 2D ([1], Materials and Methods), with a kernel width of 5 nm, or $\sigma = 3.5$ nm for the Gaussian distributions. The standardized KDE (D) is obtained by dividing density at ΔYZ by the distance ΔYZ, so that characteristic distances in the 2D distribution may appear as deviations from a horizontal line. (E) shows the RPD up to 30 nm for a model containing a flat horizontal line for a uniform distribution of localizations, and two peaks at characteristic distances. The function describing these peaks is the distance distribution between two Gaussian clusters of localizations in 2D[1] divided by distance, as in the standardization of the KDE (C, D). (F) shows the model of E fitted to the experimental data. In this case, the 95% confidence interval is narrower than the width of the line showing the best model fit.

Table S1. Parameters and uncertainties (1 s.d.) for the best fit RPD model (8-fold) to pairwise distances between Nup107 localizations (Fig. 2A–G).

Localization precision term	Amplitude	7.4(2) a.u.
	Spread (precision, s.d.)	3.63(5) nm
A (Cluster term)	Amplitude	15.3(2) a.u.
	Spread (s.d. of approx. Gaussian cluster)	9.6(1) nm
B–E (rotational symmetry contributions)	Diameter of structure	95.4(1) nm
	Amplitude of contributions	15.73(5) a.u.
	Spread (broadening of contributions, s.d.)	14.18(7) nm
Background term*	Onset	80(1) nm
	Gradient	0.00645(9) a.u. nm^{-1}

* An approximation reflecting the fact that the ring-like image features (nuclear pores), may be near to each other but do not overlap. The background is expected to have a linear form (isotropic in 2D) beyond the diameter of a nuclear pore, dominated by the distribution of other nuclear pores. It must also have a lower rate of increase at smaller distances, which we have approximated to zero, up to an 'onset' distance.

Table S2. Parameters and uncertainties for the two-layer RPD model for pairwise distances in *Z* between Nup107 localizations (Fig. 2H–L). The model contains two layers of localizations, each with the same Gaussian spread, and an exponentially decaying background. This background distribution for Δ*Z* has the same form as the distribution in *Z* of the probability of excitation in the evanescent illumination field of the TIRF instrumentation[12].

Two-layer components*	Separation between layers	58.0(1) nm
	Spread of layer (s.d.)	15.92(4)nm
	Within-layer term: amplitude	46.8(8) a.u.
	Between-layer term: amplitude	39.6(5) a.u.
Background term†	Amplitude	0.21(3) a.u.
	Exponential scale parameter	71(5) nm

* The model contains two layers of localizations in *Z*, each with the same Gaussian spread.
† An exponentially decaying background model for Δ*Z*. This has the same form as the distribution in *Z* of the probability of excitation in the evanescent illumination field of the TIRF instrumentation [12].

Table S3. Parameters and uncertainties for the best fit RPD model (8-fold) to pairwise distances between Nup107 localizations assumed to be within the same layer of the Nup107 complex (ΔZ < 20 nm).

Localization precision term	Amplitude	18.8(4) a.u.
	Spread (precision, s.d.)	3.64(3) nm
A (cluster term)	Amplitude	16.2(4) a.u.
	Spread (s.d. of approx. Gaussian cluster)	9.1(2) nm
B–E (rotational symmetry contributions)	Diameter of structure	95.5(1) nm
	Amplitude of contributions	15.52(8)a.u.
	Spread (broadening of contributions, s.d.)	13.5(1) nm
Background term	Onset	83(2) nm
	Gradient	0.0056(2) a.u. nm^{-1}

Table S4. Akaike information and weightings (summing to one) of the relative likelihood of RPD models to be the closest to the true RPD, for the models in Fig. S3.

RPD model	AICc	Akaike weight
Triangular prism on square lattice (all sides equal)*	-1748.53	0.75†
Triangular prism on square lattice (unequal sides)*	-1746.33	0.25
Cuboid on square lattice	-1477.75	1.2×10^{-59}
Tetrahedron on square lattice	-1438.53	3.6×10^{-68}

* Side length in the model with all sides of equal length was 105.5(4) nm, while the two side-lengths in the unequal-sides model were 105(1) nm and 106(2) nm. These have therefore resulted in essentially the same model, but the AICc has penalized the model that allows unequal side-lengths for having an extra parameter, and results in the selection of the more parsimonious model with all sides equal.

† Selected model.

Table S5. Parameters and uncertainties for the most likely RPD model (triangular prism, equal sides) to the distribution of pairwise distances between DNA-PAINT localizations of labelled DNA-origami structures.

Localization precision term	Amplitude	8(3) a.u.
	Spread (precision, s.d.)	4(3) nm
Inter-vertex distances	Length of edges on triangular face	105.5(4) nm
	Amplitude of contributions	2.49(5) a.u.
	Spread (broadening of contributions, s.d.)	19.9(3) nm
Substructure at vertices	Amplitude of contribution	15.7(4) a.u.
	Spread (cluster size, s.d.)	14.3(3) nm
Square lattice arrangement of prisms*	Square side length	311(23) nm
	Amplitude of contribution	325(125) a.u. nm^{-1}
	Spread (s.d., due to the prism structure at each lattice point)	72(11)
Background term	Gradient	3.3(2) $\times 10^{-3}$ a.u. nm^{-1}

* These parameters are less well-estimated, since the relevant features reflecting the lattice spacing would be beyond the maximum fitted distance on the distance histogram. However, inclusion of the features in this way did allow the models to fit to the increase in the distance histogram from 200 to 250 nm.

Table S6. Data collection, processing and refinement statistics for α-actinin-2:Affimer complexes.

	ACTN2:AF9
Source	Diamond beamline i04-1
Wavelength (Å)	0.9159
Resolution range (Å)	73.50–1.20 (1.23–1.20)*
Space group	$P2_12_12_1$
Unit-cell parameters (Å)	a=46.2, b=48.5, c=147.0
Completeness (%)	98.9 (93.3)
No. of observed reflections	603488 (23921)
No. of unique reflections	103011(7078)
Redundancy	5.9 (3.4)
$< I/\sigma(I) >$	10.4 (1.6)
Wilson B factor	13.5
R_{merge} (%)†	7.3 (80.2)
R_{pim} (%)‡	2.9 (49.3)
$CC_{1/2}$	0.99 (0.62)
Refinement statistics	
Resolution range for refinement (Å)	73.5–1.2
R factor (%)	14.9
R_{free} (%)§	16.4
No. of protein non-H atoms	1848
No. of water molecules	230
R.m.s.d bond lengths (Å)	0.008
R.m.s.d bond angles (°)	1.4
Average overall *B* factor (Å^2)	
All atoms	22.9
Protein	22.1
Water	32.0
Ramachandran analysis, the percentage of residues in the regions of plot (%)	
Favored region	97.5
Outliers	0.3
PDB code	6SWT

*Values given in parentheses correspond to those in the outermost shell of the resolution range.

† $R_{merge} = \sum_{hkl}\sum_i \left| I_i(hkl) - \langle I(hkl) \rangle \right| / \sum_{hkl}\sum I_i(hkl)$

‡ $R_{pim} = \sum_{hkl} \{1/[N(hkl)-1]\}^{1/2} \sum_i \left| I_i(hkl) - \langle I(hkl) \rangle \right| / \sum_{hkl}\sum_i I_i(hkl)$

§ R_{free} was calculated with 5% of the reflections set aside randomly.
¶ Ramachandran analysis using the program MolProbity [33].

Table S7. Akaike information and weightings (summing to one) of the relative likelihood of RPD models to be the closest to the true RPD, for pairwise distances along the cell-axis between localizations of the ACTN2 Affimer.

Axial RPD model	Fitted axial repeating distance	AICc	Akaike weight*
Linear repeat with 4 peaks (5-layer Z-disc)	18.4(6) nm	364.35	0.427
Linear repeat with 5 peaks (6-layer Z-disc)	18.5(5) nm	364.51	0.394
Linear repeat with 3 peaks (4-layer Z-disc)	18.6(7) nm	366.38	0.155
Linear fit only (Random distribution)	N/A	370.28	0.022
Linear fit, with repeated localizations also allowed	N/A	374.67	0.002

* The models for a repeating distance along the cell-axis for ACTN2 are far more likely than the model for random distribution of localizations through the thickness of the Z-disc (linear fit), or the same but including repeated localizations (or clusters) of molecules. Furthermore, these fits all resulted in the same repeating distance for ACTN2 along the direction cell-axis, close to the 19.2 nm result measured previously by EM [34]. They may be grouped together to give a combined weighting of 0.98 compared with 0.02 for the random distribution model [4, 5]. Combining the uncertainties for the linear repeat models gives a repeat of 18.5(1.0) nm.

Table S8. Parameters and uncertainties for the RPD model with highest likelihood (linear repeat with 4 peaks, 5-layer Z-disc) for the distribution of pairwise distances along the cell-axis between localizations of the ACTN2 Affimer.

Linear term (background)	Offset	49(15)a.u.
	Slope	-0.35(17)a.u. nm^{-1}
Peaks on linear repeat, height decreasing with distance	Linear repeat distance	18.4(6) nm
	Amplitude of first peak	200(236)a.u.
	Spread (broadening of peaks, s.d.)	5.3(2.0)nm
Localization precision term	Amplitude	101(126)a.u.
	Spread (precision, s.d.)	2.9(1.7)nm

Table S9: Parameters and uncertainties for the RPD model for cell-transverse pairwise distances in *YZ* between ACTN2 localizations in the cardiomyocyte Z-disc (Fig. 4D, Fig. S7).

Background	Constant value		10.587(8)a.u.
Characteristic distances (peaks)	Peak 1	Mean pairwise distance	11.17(1)nm
		Amplitude	130(2)a.u.
	Peak 2	Mean pairwise distance	24.08(5)nm
		Amplitude	203(3) a.u.
	Spread (broadening of peaks, s.d.)		5.82(2)nm

SI References

1. Churchman, L. S.; Flyvbjerg, H.; Spudich, J. A., A Non-Gaussian Distribution Quantifies Distances Measured with Fluorescence Localization Techniques. *Biophys J* **2006**, *90* (2), 668-671.
2. Fox-Roberts, P.; Marsh, R.; Pfisterer, K.; Jayo, A.; Parsons, M.; Cox, S., Local dimensionality determines imaging speed in localization microscopy. *Nat Commun* **2017**, *8*, 13558.
3. Akaike, H., Information theory as an extension of the maximum likelihood principle. In *Second International Symposium on Information Theory*, B.N Petrov, F. C., Ed. Akadémiai Kiadó: Tsahkadsor, Armenia, USSR, 1973; pp 267-281.
4. Burnham, K. P.; Anderson, D. R., *Model selection and inference: a practical information-theoretic approach*. Springer-Verlag: New York, 1998.
5. Portet, S., A primer on model selection using the Akaike Information Criterion. *Infect Dis Model* **2020**, *5*, 111-128.
6. Hurvich, C. M.; Tsai, C. L., Regression and Time-Series Model Selection in Small Samples. *Biometrika* **1989**, *76* (2), 297-307.
7. Bozdogan, H., Model selection and Akaike's Information Criterion (AIC): The general theory and its analytical extensions. *Psychometrika* **1987**, *52* (3), 345-370.
8. von Appen, A.; Kosinski, J.; Sparks, L.; Ori, A.; DiGuilio, A. L.; Vollmer, B.; Mackmull, M.-T.; Banterle, N.; Parca, L.; Kastritis, P.; Buczak, K.; Mosalaganti, S.; Hagen, W.; Andres-Pons, A.; Lemke, E. A.; Bork, P.; Antonin, W.; Glavy, J. S.; Bui, K. H.; Beck, M., In situ structural analysis of the human nuclear pore complex. *Nature* **2015**, *526*, 140.
9. Iinuma, R.; Ke, Y.; Jungmann, R.; Schlichthaerle, T.; Woehrstein, J. B.; Yin, P., Polyhedra Self-Assembled from DNA Tripods and Characterized with 3D DNA-PAINT. **2014**, *344* (6179), 65-69.
10. Schnitzbauer, J.; Strauss, M. T.; Schlichthaerle, T.; Schueder, F.; Jungmann, R., Super-resolution microscopy with DNA-PAINT. *Nat. Protocols* **2017**, *12* (6), 1198-1228.
11. Virtanen, P.; Gommers, R.; Travis E. Oliphant; Matt Haberland; Tyler Reddy; David Cournapeau; Evgeni Burovski; Pearu Peterson; Warren Weckesser; Jonathan Bright; Stéfan J. van der Walt; Matthew Brett; Joshua Wilson; K. Jarrod Millman; ikolay Mayorov; Andrew R. J. Nelson; Eric Jones; Robert Kern; Eric Larson; CJ Carey; İlhan Polat; Yu Feng; Eric W. Moore; Jake VanderPlas; Denis Laxalde; Josef Perktold; Robert Cimrman; Ian Henriksen; E.A. Quintero; Charles R Harris; Anne M. Archibald; Antônio H. Ribeiro; Fabian Pedregosa; Paul van Mulbregt; Contributors, S., SciPy 1.0--Fundamental Algorithms for Scientific Computing in Python. In *arXiv*, 2019.
12. Li, Y.; Mund, M.; Hoess, P.; Deschamps, J.; Matti, U.; Nijmeijer, B.; Sabinina, V. J.; Ellenberg, J.; Schoen, I.; Ries, J., Real-time 3D single-molecule localization using experimental point spread functions. *Nat Methods* **2018**, *15* (5), 367-369.
13. Otsuka, S.; Bui, K. H.; Schorb, M.; Hossain, M. J.; Politi, A. Z.; Koch, B.; Eltsov, M.; Beck, M.; Ellenberg, J., Nuclear pore assembly proceeds by an inside-out extrusion of the nuclear envelope. *Elife* **2016**, *5*.

14. Huang, B.; Wang, W.; Bates, M.; Zhuang, X., Three-dimensional super-resolution imaging by stochastic optical reconstruction microscopy. *Science* **2008**, *319* (5864), 810-3.
15. Carrington, G.; Tomlinson, D.; Peckham, M., Exploiting nanobodies and Affimers for superresolution imaging in light microscopy. *Mol Biol Cell* **2019**, *30* (22), 2737-2740.
16. Tiede, C.; Bedford, R.; Heseltine, S. J.; Smith, G.; Wijetunga, I.; Ross, R.; AlQallaf, D.; Roberts, A. P.; Balls, A.; Curd, A.; Hughes, R. E.; Martin, H.; Needham, S. R.; Zanetti-Domingues, L. C.; Sadigh, Y.; Peacock, T. P.; Tang, A. A.; Gibson, N.; Kyle, H.; Platt, G. W.; Ingram, N.; Taylor, T.; Coletta, L. P.; Manfield, I.; Knowles, M.; Bell, S.; Esteves, F.; Maqbool, A.; Prasad, R. K.; Drinkhill, M.; Bon, R. S.; Patel, V.; Goodchild, S. A.; Martin-Fernandez, M.; Owens, R. J.; Nettleship, J. E.; Webb, M. E.; Harrison, M.; Lippiat, J. D.; Ponnambalam, S.; Peckham, M.; Smith, A.; Ferrigno, P. K.; Johnson, M.; McPherson, M. J.; Tomlinson, D. C., Affimer proteins are versatile and renewable affinity reagents. *Elife* **2017**, *6*.
17. Haywood, N. J.; Wolny, M.; Rogers, B.; Trinh, C. H.; Shuping, Y.; Edwards, T. A.; Peckham, M., Hypertrophic cardiomyopathy mutations in the calponin-homology domain of ACTN2 affect actin binding and cardiomyocyte Z-disc incorporation. *The Biochemical journal* **2016**, *473* (16), 2485-93.
18. Bedford, R.; Tiede, C.; Hughes, R.; Curd, A.; McPherson, M. J.; Peckham, M.; Tomlinson, D. C., Alternative reagents to antibodies in imaging applications. *Biophysical Reviews* **2017**, *9* (4), 299-308.
19. Schlichthaerle, T.; Eklund, A. S.; Schueder, F.; Strauss, M. T.; Tiede, C.; Curd, A.; Ries, J.; Peckham, M.; Tomlinson, D. C.; Jungmann, R., Site-Specific Labeling of Affimers for DNA-PAINT Microscopy. *Angew Chem Int Ed Engl* **2018**, *57* (34), 11060-11063.
20. Wolny, M.; Colegrave, M.; Colman, L.; White, E.; Knight, P. J.; Peckham, M., Cardiomyopathy mutations in the tail of beta-cardiac myosin modify the coiled-coil structure and affect integration into thick filaments in muscle sarcomeres in adult cardiomyocytes. *The Journal of biological chemistry* **2013**, *288* (44), 31952-62.
21. Shroff, H.; Galbraith, C. G.; Galbraith, J. A.; White, H.; Gillette, J.; Olenych, S.; Davidson, M. W.; Betzig, E., Dual-color superresolution imaging of genetically expressed probes within individual adhesion complexes. *Proc Natl Acad Sci USA* **2007**, *104* (51), 20308-20313.
22. Lopata, A.; Hughes, R.; Tiede, C.; Heissler, S. M.; Sellers, J. R.; Knight, P. J.; Tomlinson, D.; Peckham, M., Affimer proteins for F-actin: novel affinity reagents that label F-actin in live and fixed cells. *Sci Rep* **2018**, *8* (1), 6572.
23. York, A. G.; Ghitani, A.; Vaziri, A.; Davidson, M. W.; Shroff, H., Confined activation and subdiffractive localization enables whole-cell PALM with genetically expressed probes. *Nat Methods* **2011**, *8* (4), 327-333.
24. Deschout, H.; Cella Zanacchi, F.; Mlodzianoski, M.; Diaspro, A.; Bewersdorf, J.; Hess, S. T.; Braeckmans, K., Precisely and accurately localizing single emitters in fluorescence microscopy. *Nat Methods* **2014**, *11* (3), 253-66.

25. Winter, G.; Waterman, D. G.; Parkhurst, J. M.; Brewster, A. S.; Gildea, R. J.; Gerstel, M.; Fuentes-Montero, L.; Vollmar, M.; Michels-Clark, T.; Young, I. D.; Sauter, N. K.; Evans, G., DIALS: implementation and evaluation of a new integration package. *Acta Crystallogr D Struct Biol* **2018**, *74* (Pt 2), 85-97.
26. Evans, P. R.; Murshudov, G. N., How good are my data and what is the resolution? *Acta Crystallogr D Biol Crystallogr* **2013**, *69* (Pt 7), 1204-14.
27. Potterton, L.; Agirre, J.; Ballard, C.; Cowtan, K.; Dodson, E.; Evans, P. R.; Jenkins, H. T.; Keegan, R.; Krissinel, E.; Stevenson, K.; Lebedev, A.; McNicholas, S. J.; Nicholls, R. A.; Noble, M.; Pannu, N. S.; Roth, C.; Sheldrick, G.; Skubak, P.; Turkenburg, J.; Uski, V.; von Delft, F.; Waterman, D.; Wilson, K.; Winn, M.; Wojdyr, M., CCP4i2: the new graphical user interface to the CCP4 program suite. *Acta Crystallogr D Struct Biol* **2018**, *74* (Pt 2), 68-84.
28. McCoy, A. J.; Grosse-Kunstleve, R. W.; Adams, P. D.; Winn, M. D.; Storoni, L. C.; Read, R. J., Phaser crystallographic software. *J Appl Crystallogr* **2007**, *40* (Pt 4), 658-674.
29. Tiede, C.; Tang, A. A.; Deacon, S. E.; Mandal, U.; Nettleship, J. E.; Owen, R. L.; George, S. E.; Harrison, D. J.; Owens, R. J.; Tomlinson, D. C.; McPherson, M. J., Adhiron: a stable and versatile peptide display scaffold for molecular recognition applications. *Protein engineering, design & selection : PEDS* **2014**, *27* (5), 145-55.
30. Cowtan, K., Fitting molecular fragments into electron density. *Acta Crystallogr D Biol Crystallogr* **2008**, *64* (Pt 1), 83-9.
31. Emsley, P.; Lohkamp, B.; Scott, W. G.; Cowtan, K., Features and development of Coot. *Acta Crystallogr D Biol Crystallogr* **2010**, *66* (Pt 4), 486-501.
32. Kovalevskiy, O.; Nicholls, R. A.; Long, F.; Carlon, A.; Murshudov, G. N., Overview of refinement procedures within REFMAC5: utilizing data from different sources. *Acta Crystallogr D Struct Biol* **2018**, *74* (Pt 3), 215-227.
33. Chen, V. B.; Arendall, W. B., 3rd; Headd, J. J.; Keedy, D. A.; Immormino, R. M.; Kapral, G. J.; Murray, L. W.; Richardson, J. S.; Richardson, D. C., MolProbity: all-atom structure validation for macromolecular crystallography. *Acta Crystallogr D Biol Crystallogr* **2010**, *66* (Pt 1), 12-21.
34. Burgoyne, T.; Morris, E. P.; Luther, P. K., Three-Dimensional Structure of Vertebrate Muscle Z-Band: The Small-Square Lattice Z-Band in Rat Cardiac Muscle. *J Mol Biol* **2015**, *427* (22), 3527-3537.
35. Sieben, C.; Banterle, N.; Douglass, K. M.; Gönczy, P.; Manley, S., Multicolor single-particle reconstruction of protein complexes. *Nature Methods* **2018**, *15* (10), 777-780.
36. Douglass, K. M.; Sieben, C.; Archetti, A.; Lambert, A.; Manley, S., Super-resolution imaging of multiple cells by optimized flat-field epi-illumination. *Nat Photon* **2016**, *10* (11), 705-708.
37. Edelstein, A.; Amodaj, N.; Hoover, K.; Vale, R.; Stuurman, N., Computer control of microscopes using microManager. *Curr Protoc Mol Biol* **2010**, *Chapter 14*, Unit14 20.

38. Olivier, N.; Keller, D.; Gonczy, P.; Manley, S., Resolution doubling in 3D-STORM imaging through improved buffers. *PloS one* **2013**, *8* (7), e69004.
39. Huang, F.; Hartwich, T. M.; Rivera-Molina, F. E.; Lin, Y.; Duim, W. C.; Long, J. J.; Uchil, P. D.; Myers, J. R.; Baird, M. A.; Mothes, W.; Davidson, M. W.; Toomre, D.; Bewersdorf, J., Video-rate nanoscopy using sCMOS camera-specific single-molecule localization algorithms. *Nat Methods* **2013**, *10* (7), 653-8.